Structural and magnetic properties of holmium-scandium alloys and superlattices

C. Bryn-Jacobsen and R. A. Cowley
Oxford Physics, Clarendon Laboratory, Parks Road, Oxford, OX1 3PU, United Kingdom

D. F. McMorrow
Department of Solid State Physics, Risø National Laboratory, DK-4000 Roskilde, Denmark

J. P. Goff, R. C. C. Ward, and M. R. Wells
Oxford Physics, Clarendon Laboratory, Parks Road, Oxford, OX1 3PU, United Kingdom

(Received 30 July 1996)

The properties of Ho-Sc alloys and superlattices grown by molecular-beam epitaxy have been investigated using x-ray and neutron-diffraction techniques. Structural studies reveal that the alloy samples have different a lattice parameters for the Sc-seed layer and the Ho:Sc alloy grown on top of the seed layer; while the superlattices have different a lattice parameters for the Sc seed, and for *both* the Ho and Sc in the superlattice layers. The structural characteristics are related to the large lattice mismatches (of the order 7%) between the constituent elements. The magnetic moments in the alloys form a basal-plane helix at all temperatures, with distortions of the helical arrangement for samples with the highest Ho concentrations. The dependences of the Néel temperature, T_N, and the helical wave vector upon both temperature and concentration are compared with those of other alloy systems. It is found that a good description of the dependence of T_N upon concentration is given by a virtual-crystal model where the peak in the conduction-electron susceptibility varies linearly between that of the pure constituents. In the superlattices, the moments also form a basal-plane helix at T_N. In this helical phase, some samples exhibit a short-range coherence of an antiferromagnetic coupling between adjacent Ho blocks. For one superlattice, there is a low-temperature transition to a ferromagnetic phase, in which moments are ferromagnetically aligned within Ho blocks, and coupled antiferromagnetically between adjacent Ho blocks. The contrast with systems which have Y or Lu as the nonmagnetic element is discussed in terms of the structural properties of the samples, band-structure calculations, and the possible influence of dipolar forces. [S0163-1829(97)04401-9]

I. INTRODUCTION

There have recently been extensive studies of alloy and superlattice systems grown by molecular-beam epitaxy (MBE). Of particular interest are rare-earth-based systems, many of which were reviewed by Majkrzak *et al.*,[1] Rhyne *et al.* ,[2] and Cowley *et al.*[3] These investigations have revealed considerable departures both from bulk structural and magnetic properties.

The experimental results from these systems have raised questions concerning conventional theories used to describe magnetic interactions in rare earths. This is illustrated for magnetic:nonmagnetic alloys by considering the variation of Néel temperature, T_N, with the concentration of magnetic element x. In early studies of many alloy systems,[4] T_N was found to be a universal function of the de Gennes factor. However, Swaddling *et al.*[5] carried out a detailed study of MBE-grown Ho:Y and Ho:Lu alloys, and found a different dependence of T_N upon x. Investigations involving other Ho-based alloy systems would thus be particularly useful for comparison.

Theoretical interpretations of the magnetic ordering of rare-earth superlattices were originally based upon conventional Ruderman-Kittel-Kasuya-Yosida theory,[6] in which $4f$ moments spin polarize the $5d$ and $6s$ conduction electrons. These electrons gain a magnetization similar in form to the ordered moments, and propagate through the material interacting with other $4f$ moments. In a magnetic/nonmagnetic superlattice, moments in a magnetic block spin polarize the conduction electrons in the adjacent nonmagnetic block. The form of the induced polarization in the nonmagnetic region is determined by the conduction-electron susceptibility $\chi(\boldsymbol{q})$. This induced spin-density wave mediates the coupling between the magnetic blocks that is necessary for the establishment of coherent magnetic order. The range of the interaction is calculated from the Fourier transform of $\chi(\boldsymbol{q})$, which depends upon the band structure. This model was used to describe the magnetic properties of some of the first superlattices, such as Gd/Y (Ref. 6) and Dy/Y.[6] However, it has proved more difficult to reconcile the results from some recent studies with the theory in this form. For example, in Ho/Er (Ref. 7) superlattices, no long-range coherence was found for the c-axis component of the Er moments over intermediate Ho blocks. Similarly for Ho/Pr,[8] no coherent ordering of Ho moments across Pr layers was observed. The further example of Dy/Sc (Ref. 9) is of special relevance. Band-structure calculations[10] suggest that Sc has a conduction-electron susceptibility along the c axis that is qualitatively similar to that of Y. Given these calculations, and also the long-ranged order of Dy moments observed in Dy/Y (Ref. 11) superlattices, coherent ordering of the Dy moments through the Sc layers might have been expected. No coherence was detected though, suggesting that there would be considerable interest in investigating other superlattices with Sc interlayers.

In this paper, we present a comprehensive study of MBE grown Ho-Sc alloys and superlattices. Bulk Ho and Sc have the hexagonal-close-packed (hcp) crystal structure[12] with an $ABAB\ldots$ stacking of close-packed planes. The lattice parameters for Sc relative to Ho (Ref. 12) are such that $\Delta a/a=-7.5\%$ and $\Delta c/c=-6.1\%$, compared to values for Sc relative to Dy (Ref. 9) of $\Delta a/a=-7.8\%$ and $\Delta c/c-6.6\%$. These percentages are particularly large compared with values of $\Delta a/a$ and $\Delta c/c$ for other superlattice systems; for instance Y relative to Ho (Ref. 13) ($+2.0\%$, $+2.0\%$), Lu relative to Ho (Ref. 13) (-2.1%, -1.2%), or even Pr relative to Ho (Ref. 8) ($+2.3\%$, $+5.4\%$). The large lattice mismatches for Ho-Sc are an important factor in determining the structural characteristics of the system.

The magnetic properties of the rare earth Ho have been well documented. Koehler *et al.*[14] established that between $T_N=132.2$ K and $T\approx 18$ K, the $4f$ moments align in the basal plane. The moments are ferromagnetically coupled within each basal plane, and their orientation rotates between successive planes along the c axis. The wave vector of the helix reduces smoothly on cooling from $\boldsymbol{q}=0.271\boldsymbol{c}^*$ at T_N to $\boldsymbol{q}=(1/6)\boldsymbol{c}^*$ below $T\approx 18$ K, when the moments also tilt out of the basal plane to form a ferromagnetic cone structure. Gibbs *et al.*[15] used x-ray magnetic scattering to investigate the ordering more thoroughly, and found that between $T\approx 30$ and 18 K, the wave vector locks in to a series of values commensurable with the crystal lattice. These lock-ins were studied in detail by Cowley and Bates[16] using neutron-scattering techniques, with a further examination of the low-temperature magnetic structures undertaken by Simpson *et al.*[17] The transition metal Sc is nonmagnetic, but its outer electron configuration of $3d4s^2$ is similar to Y, Lu, and the heavy rare-earth elements.[10]

In the 1960's, Child and Koehler[18] obtained powder neutron-diffraction patterns from alloy samples of Ho with Sc. They found that the Ho $4f$ moments ordered in a helical structure, with no ferromagnetic component. MBE can now be used to produce highly homogeneous alloys, as well as superlattice samples. To our knowledge, there have been no other studies of MBE-grown Ho-Sc alloys or superlattices.

Sections II and III give accounts of the growth and experimental procedures used for examining the Ho-Sc system. These are followed in Sec. IV with a presentation of the structural investigations of the samples, describing the results first from the alloys, and then from the superlattices. Section V details the elucidation of the magnetic properties, and is similarly divided into subsections for alloys and superlattices. To conclude, in Sec. VI the implications of our results are discussed in the light of previous studies of MBE-grown rare-earth alloys and superlattices.

II. SAMPLE GROWTH

The Ho-Sc samples were grown by MBE using a Balzers UMS 630 facility at the Clarendon Laboratory, Oxford, adopting the growth techniques developed by Kwo *et al.*,[19] and described by Jehan *et al.*[20] For each sample, a sapphire substrate was used (with a surface area measuring approximately 1 cm^2), upon which was deposited 1500 Å of body-centered-cubic (bcc) Nb as a chemical buffer layer. This was followed by a 1800 Å Sc-seed layer to enable the lattice parameters to relax back to suitable values before growth of the rare earths. The rare-earth elements were evaporated from Knudsen effusion cells, with the cell temperature being flux calibrated using an *in situ* quartz crystal monitor before each run to produce samples of designated compositions. A 250 Å Sc-capping layer was then added for general protection and in particular to reduce oxidation. In the growth direction, the epitaxial relationships are $(11\bar{2}0)Al_2O_3\|\ (110)Nb\ \|\ (0001)Sc\text{-}Ho$. The in-plane epitaxial relationships between (110)Nb and $(11\bar{2}0)Al_2O_3$ are $[\bar{1}11]Nb\ \|\ [0001]Al_2O_3$, and $[1\bar{1}2]Nb\ \|\ [10\bar{1}0]Al_2O_3$. For the in-plane orientation of the (0001)rare earth and the $(11\bar{0})$Nb it is found that the most densely packed row $[11\bar{2}0]$rare earth is parallel to the densely packed row of [002]Nb, and in the orthogonal direction the $[10\bar{1}0]$rare earth is parallel to $[1\bar{1}0]$Nb. Henceforth, we shall refer to, say, [0001] and (0001) as [001] and (001), respectively.

When growing the alloys, the substrate temperature was $T=700\ ^\circ$C, which was chosen to be high enough to promote both good crystallinity and bulk interdiffusion. For each sample, the (typically) 10 000 Å of the rare-earth alloy was grown at a combined rare-earth evaporation rate of 1 Å s^{-1}. The six samples produced, $Ho_x:Sc_{1-x}$, have nominal Ho concentrations of $x=0.25$, 0.40, 0.50, 0.75, 0.85, and 1.00.

The substrate temperature was reduced to $T=400\ ^\circ$C for the growth of the superlattices to allow sufficient surface mobility to encourage layer-by-layer growth, while limiting the extent of interfacial interdiffusion.[21] Ho and Sc were evaporated alternately at a rate of 0.5 Å s^{-1}. The three samples grown, $(Ho_{n_{Ho}}/Sc_{n_{Sc}})_N$, have nominal compositions of $(Ho_{30}/Sc_{10})_{80}$, $(Ho_{20}/Sc_{20})_{80}$, and $(Ho_{20}/Sc_{40})_{60}$, for n_{Ho} and n_{Sc} planes of Ho and Sc in a single bilayer, with the bilayer unit repeated N times.

III. EXPERIMENTAL PROCEDURES

The samples were examined at the Clarendon Laboratory, Oxford using a high-resolution triple-axis x-ray diffractometer mounted on a Stöe rotating anode generator, operating at 6 kW. At room temperature, scans were performed with the wave-vector transfer $\boldsymbol{Q}$ along the $[00\ell]$ direction in reciprocal space, in addition to transverse scans through the main (002) nuclear Bragg peak.

Neutron-scattering experiments were undertaken at Risø National Laboratory, Denmark, using triple-axis spectrometers situated on the cold source of the DR3 reactor. Samples were all mounted with the $(h0\ell)$ plane in the scattering plane, and $\boldsymbol{Q}$ was scanned along the directions $[00\ell]$, $[h00]$, and $[10\ell]$. The alloys were placed in a closed-cycle cryostat for temperature measurements in the range $T=10$–140 K, while the superlattices were positioned in a variable-flow cryostat for measurements between $T=4$ and 140 K. Temperatures could be measured to an accuracy of approximately ± 1 K. Pyrolytic-graphite crystals were used as monochromator and analyzer, both being set to reflect 5 meV neutrons. The reactor-to-sample horizontal collimations of $120'-30'-60'-140'$ for the alloys, and $30'-40'-60'-81'-141'$ for the superlattices, resulted in wave-vector resolutions in the scattering plane of approxi-

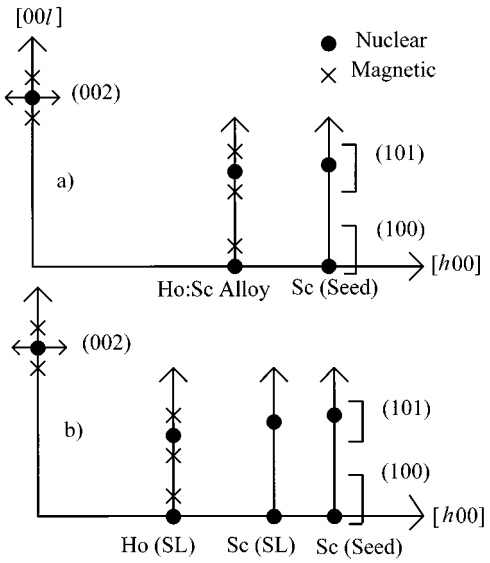

FIG. 1. A schematic diagram of reciprocal space (not to scale) showing the scan directions used in structural and magnetic investigations of (a) the alloy, and (b) the superlattice samples. Filled circles represent nuclear Bragg peaks, while crosses indicate regions where magnetic scattering would be detected for a helical arrangement of Ho moments. The FWHM of scans of $\boldsymbol{Q}$ along [00ℓ] through the (002) nuclear Bragg peak can be used to find the coherence of the stacking of closed-packed planes. Transverse scans through the (002) peak give an indication of sample quality. Scans of $\boldsymbol{Q}$ along [h00] reveal the existence of more than one a lattice parameter. For the superlattices, scans of $\boldsymbol{Q}$ in the ℓ direction with h fixed at the values of h identified from [h00] scans, can be used to give the coherence of the $ABAB\ldots$ stacking sequence of a particular sample constituent.

mately $q=0.013$ Å^{-1} and $q=0.012$ Å^{-1} [full width at half maximum (FWHM)], respectively. A cooled beryllium filter was employed to reduce higher-order contamination of the incident neutron beam.

IV. STRUCTURAL PROPERTIES

Both x-ray and neutron-diffraction techniques were used to investigate the structural characteristics of the samples. Figure 1 is a schematic diagram of reciprocal space showing the directions in which the wave-vector transfer $\boldsymbol{Q}$ was scanned to assess the structural coherence of (a) the alloys, and (b) the superlattices. Firstly, high-resolution x-ray scans were performed with $\boldsymbol{Q}$ along the [00ℓ] direction. The width of the main (002) Bragg peak obtained from these scans was used to give the real-space coherence ξ of the stacking of close-packed planes in the growth direction, since (neglecting the very high x-ray resolution) $\xi=2\pi/\Delta\boldsymbol{Q}$, where $\Delta\boldsymbol{Q}$ is the FWHM of the peak in reciprocal space. Transverse scans were made through the (002) peak and the FWHM used as a measure of sample quality, here referred to as the mosaic spread of the sample.

Secondly, studies were made using neutron scattering, with $\boldsymbol{Q}$ scanned along [h00] to investigate the in-plane structural properties of the samples. In previous MBE-grown systems, such as Ho-Y,[20,22] Ho-Lu,[5] and Ho-Pr,[8,23] scans of $\boldsymbol{Q}$ in this direction revealed a single (100) peak, indicating that within error there existed a single a lattice parameter. In contrast, for the Ho-Sc system more than one peak is detected near the expected (100) position, implying the samples did not grow pseudomorphically, and that each sample possesses more than one in-plane lattice parameter. For the alloy samples, scans of $\boldsymbol{Q}$ along [h00] reveal two (100) peaks that can be identified with the existence of different a lattice parameters for the Sc seed, and the Ho:Sc alloy. Three peaks are seen when the same scan is performed for the superlattice samples, indicating that there are different a lattice parameters for the Sc seed, the Ho in the superlattice, and the Sc in the superlattice. The directions of scans performed with h fixed at a value associated with a specific constituent will be labeled with an appropriate subscript. For example, scans of $\boldsymbol{Q}$ along ℓ for the superlattices with h fixed at the value of h for the (100) peak of Ho, will be referred to as $[10\ell]_{\mathrm{Ho}}$. Having identified the relevant h values for the superlattice samples, scans of $\boldsymbol{Q}$ along ℓ were carried out with h fixed at these values, to find the coherence of the hcp $ABAB\ldots$ stacking sequence for the different sample constituents.

A. Ho:Sc alloys

Studies of the alloys using x-ray scattering techniques yield structural coherence lengths in the growth direction of $\xi>2000$ Å, and typical mosaic spreads of 0.1°, as documented in Table I. These values are comparable with those

TABLE I. The structural properties of Ho:Sc alloys. The fitted compositions were deduced by comparing the results from lattice parameter measurements using both x rays and neutrons, with Vegard's Law, as described in Sec. IV A. The a and c lattice parameters listed are those obtained at $T=300$ K using x-ray diffraction. The mosaic spread values are the FWHM of transverse x-ray scans through the (002) nuclear Bragg peak. The coherence lengths refer to structural coherence in the growth direction, as determined from x-ray measurements.

Nominal x	Fitted $x\pm0.03$	Nominal thickness Å	a ±0.001 Å	$c/2$ ±0.0005 Å	Mosaic spread $\pm0.03°$	Coherence length ±100 Å
0.25	0.18	10 000	3.363	2.6622	0.11	2850
0.40	0.33	10 000	3.403	2.6857	0.15	3750
0.50	0.40	10 000	3.413	2.6982	0.12	2050
0.75	0.71	10 000	3.496	2.7506	0.13	3500
0.85	0.85	10 000	3.529	2.7773	0.14	3350
1.00	1.00	2800	3.565	2.8109	0.14	2500

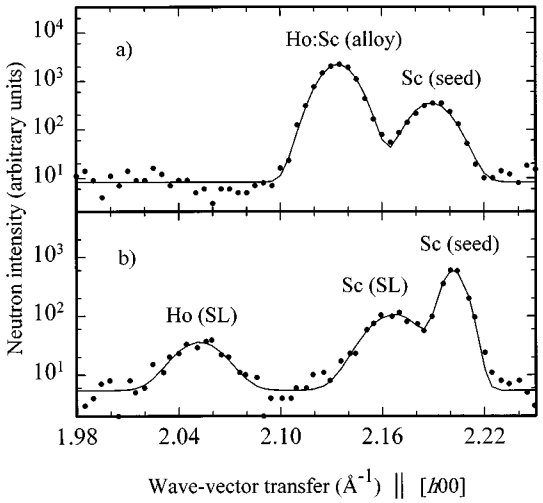

FIG. 2. Scans at $T=140$ K of the wave-vector transfer, $\boldsymbol{Q}$, along $[h00]$ using neutrons, showing that separate a lattice parameters exists for the (a) alloy, and (b) superlattice samples.

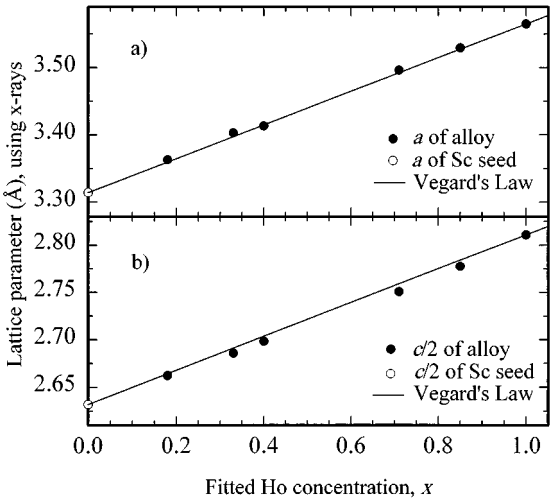

FIG. 3. (a) The a and (b) the c lattice parameters of the alloy samples as measured at $T=300$ K using x rays. The straight line is an extrapolation between values for $x=1.00$ and the Sc seed value of $x=0.00$, which gives the dependence of the lattice parameters upon concentration for alloys obeying Vegard's Law.

obtained from previous alloy systems[22] grown using similar methods.

Measurements of the neutron scattering when $\boldsymbol{Q}$ is scanned in the $[h00]$ direction reveal two (100) Bragg peaks, which indicates that the samples have different a lattice parameters for the Sc-seed layer and the Ho:Sc alloy. A typical scan is shown in Fig. 2(a).

A number of methods were considered to refine the nominal compositions, including comparisons of the integrated intensities of nuclear and magnetic Bragg peaks, examinations of the lattice parameters obtained from both x-ray and neutron-scattering measurements, as well as noting trends in magnetic ordering temperatures and wave vectors. The refinement was made using the lattice parameter data obtained from neutron measurements at $T=140$ K (where $T>T_N$). Fitted compositions were derived by comparing the measurements with a linear extrapolation between the values for $x=1.00$ and $x=0.00$ (the Sc seed), as would be appropriate for alloys obeying Vegard's Law. Figure 3 is an illustration of the consistency between the lattice parameters obtained using x rays and neutrons. This figure shows the results of x-ray measurements at $T=300$ K compared to Vegard's Law, with the sample compositions set to the values obtained from the refinement based upon the neutron-scattering data. Table I lists the nominal and fitted compositions, with the agreement not being as close as that obtained for Ho:Y and Ho:Lu alloys.[5] For the Ho:Sc samples, the discrepancy between nominal and fitted compositions was traced to a calibration error arising from an incorrect positioning of the quartz crystal monitor in the MBE chamber.

B. Ho/Sc superlattices

High-resolution x-ray-scattering techniques were employed to study the structural properties of the superlattice samples. At $T=300$ K, scans of $\boldsymbol{Q}$ along the $[00\ell]$ direction reveal the main (002) Bragg peak together with a series of peaks at separations $2m\pi/L$ (where m is an integer, and L is the bilayer repeat distance in Å), and a sharp peak due to the presence of the Sc-seed and capping layers [see Fig. 4(a) for a typical example]. The intensity, $I(\boldsymbol{Q})$, of elastic scattering of x rays from a crystal lattice is given by

$$I(\boldsymbol{Q}) \propto \left| \sum_l f_l(\boldsymbol{Q}) e^{i\boldsymbol{Q}\cdot\boldsymbol{R}_l} \right|^2 , \tag{1}$$

where $\boldsymbol{Q}$ is the wave-vector transfer, $f_l(\boldsymbol{Q})$ is the scattering amplitude of the lth atom, and $\boldsymbol{R}_l$ is the position of the lth atom. The sum is over all atomic planes in the superlattice. For scans with $\boldsymbol{Q}$ along $[00\ell]$, and writing the c-axis component of $\boldsymbol{R}_l$ as R_l, Eq. (1) can be factorized into two terms such that

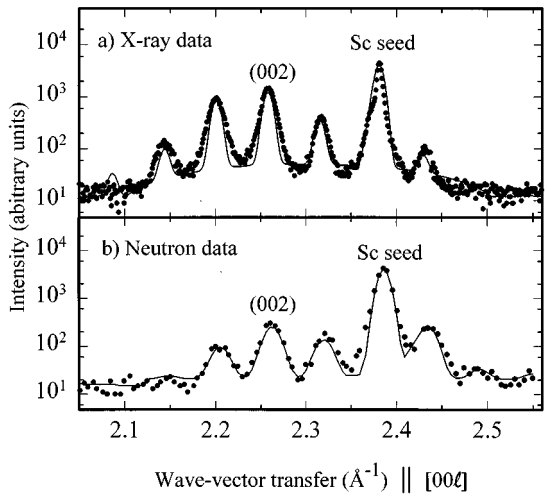

FIG. 4. Scans of $\boldsymbol{Q}$ along $[00\ell]$ through the (002) nuclear Bragg peak of the superlattice sample Ho_{20}/Sc_{20} at (a) $T=300$ K using x rays and (b) $T=140$ K using neutrons. The solid line is a fit to the data using the model described in Sec. IV B.

TABLE II. The structural properties of Ho/Sc superlattices. The fitted compositions, d spacings, and values for σ were determined by fitting the results from both x-ray and neutron-diffraction measurements of $\boldsymbol{Q}$ scanned in the direction $[00\ell]$, to models of the superlattice structure based upon the work of Jehan *et al.* (Ref. 20). Within this model, σ is a parameter associated with the width of interdiffusion at the interfaces. The mosaic spread values are the FWHM of transverse x-ray scans through the main (002) nuclear Bragg peak. The coherence lengths listed are for the structural coherence in the growth direction, and were obtained using x rays.

Nominal Ho/Sc	Fitted Ho/Sc	N	d_{Ho} ± 0.002 Å	d_{Sc} ± 0.002 Å	σ ± 1.0 plane	Mosaic spread $\pm 0.3°$	Coherence length ± 50 Å
20/20	19.0/21.5	80	2.814	2.625	1.5	2.1	450
30/10	26.5/10.0	80	2.804	2.634	2.0	1.7	650
20/40	19.5/36.0	60	2.795	2.620	2.5	1.7	450

$$I(Q)\propto\left|\left(\sum_{m=1}^{N} e^{iQLm}\right)\left(\sum_{l=0}^{\text{one bilayer}} f_l(Q)e^{iQR_l}\right)\right|^2 , \quad (2)$$

where $Q=|\boldsymbol{Q}|$, the bilayer length $L=n_{\mathrm{Ho}}d_{\mathrm{Ho}}+n_{\mathrm{Sc}}d_{\mathrm{Sc}}$, and the d spacings d_{Ho}, and d_{Sc} are the separation of close-packed planes in the growth direction of Ho and Sc, respectively. The first sum in Eq. (2) generates the series of peaks observed at positions

$$Q_{\mathrm{Nuc}}=2m\pi/L , \quad (3)$$

with the amplitude of the peaks modulated by the second term, the one-bilayer structure factor. The width of the (002) peak obtained from scans of $\boldsymbol{Q}$ along $[00\ell]$ gives a coherence of the stacking of close-packed planes in the growth direction over many bilayer repeats, as recorded in Table II. Transverse scans through the (002) peak yield mosaic spread values of approximately 2°, which is large compared to the typical range of 0.1°–0.5° for superlattices such as Ho/Y (Ref. 20) and Ho/Lu,[13] grown by the same technique. This large value is presumably connected with the considerable lattice mismatches between Ho and Sc.

Figure 2(b) illustrates the neutron scattering at $T=140$ K from a superlattice sample when $\boldsymbol{Q}$ is scanned along $[h00]$. The presence of three peaks indicates separate a lattice parameters for the Sc seed, and for *both* the Ho and Sc in the superlattice. The existence of different in-plane lattice parameters has not, to our knowledge, been reported for any previous MBE-grown rare-earth superlattices. However, the separate values of a for the Ho and Sc in the superlattice do not correspond to bulk values, implying that the system is still strained to some extent. Figure 5 shows the results of scanning $\boldsymbol{Q}$ in the ℓ direction with h fixed at values appropriate for (a) Ho in the superlattice, (b) Sc in the superlattice, and (c) the Sc seed. The widths of the peaks in (a) and (b) indicate that coherence of the hcp $ABAB\ldots$ stacking sequence is confined to individual Ho or Sc blocks. As an illustration of the different structural coherence lengths, Fig. 6 shows the results of neutron-scattering measurements at $T=4$ K where $\boldsymbol{Q}$ is scanned along (a) $[00\ell]$, and (b) $[10\ell]_{\mathrm{Ho}}$. In the former direction, there is long-range structural coherence as attested to by the presence of superlattice peaks around (002). This is to be contrasted with the scan of $\boldsymbol{Q}$ along $[10\ell]_{\mathrm{Ho}}$, where no structure is seen in the scattering near $(101)_{\mathrm{Ho}}$. The difference arises because the $[00\ell]$ scans are sensitive only to the *existence* of close-packed planes, whereas the $[10\ell]$ scans give information about the stacking sequence of the close-packed planes. The peaks marked $(002\pm q)$ and $(101\pm q)_{\mathrm{Ho}}$ are magnetic in origin, and will be discussed in the following section.

The exact composition of the samples can be determined by fitting independently scans of $\boldsymbol{Q}$ in the $[00\ell]$ direction (obtained at temperatures above the magnetic ordering temperatures) using both x rays and neutrons, to a model of the superlattice structure as described in detail by Jehan *et al.*[20] This model includes a simulation of interfacial interdiffusion using a $\tanh(z/\sigma)$ function, where z is along $[00\ell]$, and σ defines the width of the interface. The results from both the x-ray and neutron-scattering data are identical within errors, with typical fits to both sets of data shown by the solid lines in Fig. 4. For each sample, it was possible to extract values for the bilayer length, the number of planes of Ho and Sc, the d spacings for Ho and Sc, and σ. Consistent agreement was obtained between the nominal and fitted number of planes, with the results presented in Table II.

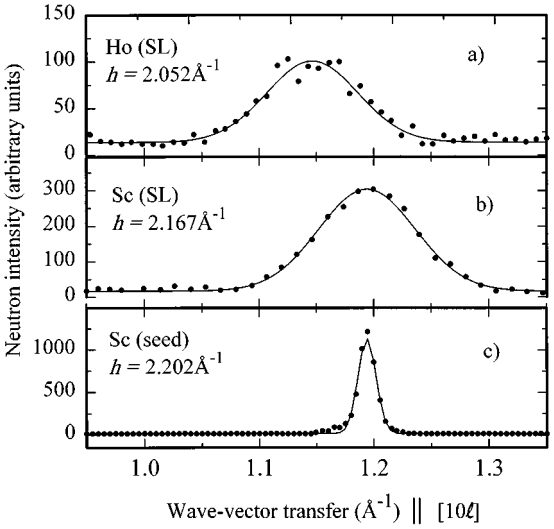

FIG. 5. Scans at $T=140$ K of $\boldsymbol{Q}$ in the ℓ direction of the superlattice sample $\mathrm{Ho}_{20}/\mathrm{Sc}_{20}$ at $T>T_{\mathrm{N}}$, where h is fixed at values appropriate for (a) Ho in the superlattice, (b) Sc in the superlattice, and (c) the Sc seed. The solid line is a fit of the data to a Gaussian function used to give the positions in h of the three peaks.

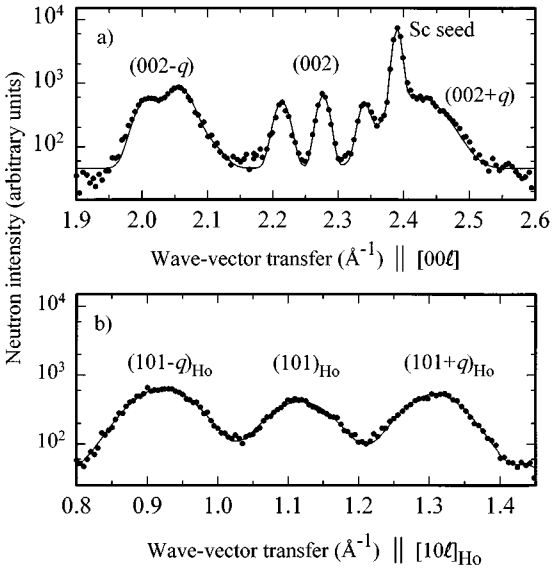

FIG. 6. The neutron scattering observed at $T=4$ K from the superlattice sample Ho_{30}/Sc_{10}. (a) A scan with $\boldsymbol{Q}$ along [00ℓ], with superlattice peaks around (002) separated by $2\pi/L$ resulting from the periodically repeated bilayer unit of length L. The width of the peaks gives a coherence of the stacking of close-packed planes over several hundred Å. The peaks at positions $(002\pm q)$ are magnetic in origin, and can be identified with a helical ordering of Ho moments. (b) A scan with $\boldsymbol{Q}$ along $[10\ell]_{Ho}$ displaying no superlattice peaks around $(101)_{Ho}$. The width of this nuclear peak indicates that the hcp stacking sequence $ABAB\ldots$ is coherent only within individual blocks. The peaks at positions $(101\pm q)_{Ho}$ again arise from a helical moment configuration, but there is no structure to suggest coherence of ordering in this direction. All solid lines are a guide to the eye.

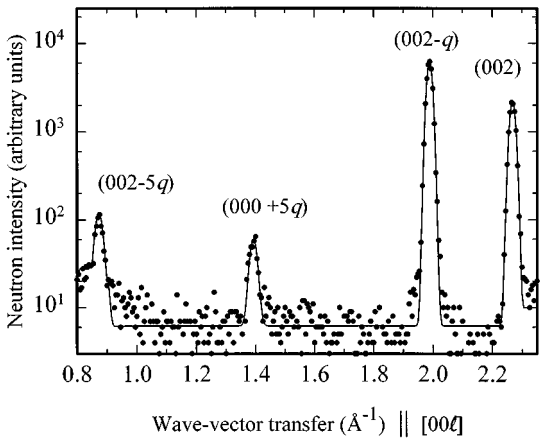

FIG. 7. The neutron scattering observed at $T=10$ K from the alloy sample with $x=0.85$ when $\boldsymbol{Q}$ is scanned along [00ℓ], showing the nuclear (002) Bragg peak, a peak at $(002-q)$ associated with a helical arrangement of moments, and the harmonics of $(002-5q)$, and $(000+5q)$ indicating that there is some distortion of the helical ordering. The solid line is a guide to the eye.

V. MAGNETIC PROPERTIES

A. Ho:Sc alloys

The magnetic properties of the alloy samples were studied using neutron-scattering techniques. Scans with $\boldsymbol{Q}$ along [00ℓ] were carried out at a number of temperatures between $T=140$ and 10 K to investigate the ordering of moments in the basal plane. At $T=140$ K, all samples exhibit only nuclear scattering. However, on reducing the temperature, additional scattering is detected with an intensity that increases smoothly with decreasing temperature. This intensity is attributable to the magnetic ordering of the Ho $4f$ moments. Figure 7 illustrates the scattering profile observed at $T=10$ K for the alloy with $x=0.85$. The peak at $(002-q)$ is present for all samples, and arises from a basal-plane helical ordering of moments, characterized by a wave vector, $\boldsymbol{q}$. The width of the $(002-q)$ peak, after allowing for instrumental resolution, can be used to give the coherence length of the magnetic ordering ξ again employing the relation $\xi=2\pi/\Delta\boldsymbol{Q}$. Except for the alloy sample with $x=1.00$ at $T=10$ K, the coherence length is found to be at least 300 Å and temperature independent. The peaks at positions $(002-5q)$ and $(000+5q)$ are observed for samples with $x>0.5$ at $T=10$ K. These higher harmonics of the principal magnetic scattering indicate that the moments no longer form regular helices, but instead bunch about the easy axes in the basal plane, as observed in pure Ho.[24] The width of these harmonics corresponds to a coherence length that is approximately 100 Å less than that derived from the $(002-q)$ peak. This reduction indicates that the details of the irregularities in the helical ordering are not coherent over as great a range as the average characteristics of the primary magnetic scattering. Scans of the wave-vector transfer along $[10\ell]_{alloy}$ were also performed at temperatures above and below T_N, being sensitive to components of the moments in the basal plane *and* along the c axis. For all samples, no extra scattering is detected around $(100)_{alloy}$ or $(101)_{alloy}$ for $T<T_N$ when compared to the results obtained near (002). We therefore conclude that the moments are predominately confined to the basal plane.

Values of T_N are listed in Table III, and were deduced from the temperature dependence of the scattering detected at the $(002-q)$ position. Figure 8 shows the variation of T_N with fitted Ho concentration x together with the results from Ho:Y and Ho:Lu alloys.[5] In early studies of many alloy systems,[4] it was found that

TABLE III. The magnetic properties of Ho:Sc alloys. The Néel temperatures T_N were calculated from the temperature dependence of the intensity of magnetic scattering measured at $(002-q)$. $\boldsymbol{q}_1$ and $\boldsymbol{q}_2$, are the wave vectors of the helical ordering at $T=T_N$ and $T=10$ K, respectively. The spin-slip model of Cowley and Bates (Ref. 16) can be used to identify the low-temperature structures to which the $\boldsymbol{q}_2$ values correspond. These structures are given in terms of the resulting fractional wave vector.

Nominal x	T_N K	$\boldsymbol{q}_1$ $\pm 0.002\boldsymbol{c}^*$	$\boldsymbol{q}_2$ $\boldsymbol{c}^*$	Spin-slip $\boldsymbol{c}^*$
0.25	14±2	0.251	0.251±0.002	1/4
0.40	29±2	0.262	0.261±0.002	6/23
0.50	35±4	0.265	0.264±0.002	5/19
0.75	74±2	0.272	0.258±0.002	8/31
0.85	98±2	0.275	0.246±0.002	14/57
1.00	132±1	0.278	0.178±0.003	7/39

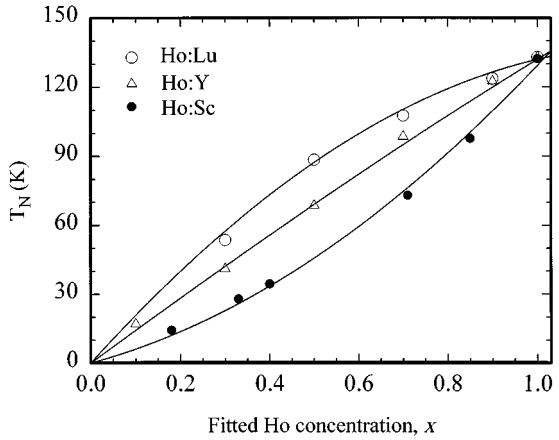

FIG. 8. The dependence of T_N upon x, where x is the fitted Ho concentration for the alloys Ho:Lu, Ho:Y, and Ho:Sc. The solid lines are a fit of the data using the relation $T_N = x[xT_{Ho} + (1-x)T_\gamma]$, as predicted by an alloy virtual-crystal model. For Ho:Lu and Ho:Y, $T_{Ho} = 132 \pm 2$ K; with $T_\gamma = 144 \pm 2$ K, and 217 ± 3 K, respectively. For Ho:Sc, $T_{Ho} = 130 \pm 2$ K, and $T_\gamma = 53 \pm 2$ K.

$$T_N \approx A y^{2/3} \quad , \tag{4}$$

where the de Gennes factor $y = x(g-1)^2 J(J+1)$, g is the Landé factor, and J is the total angular momentum of the rare-earth ion. However, Eq. (4) does not describe the detailed dependence of T_N upon x observed for Ho:Sc alloys. Swaddling *et al.*[5] found that Eq. (4) was also inappropriate for Ho:Y and Ho:Lu alloys, and proposed a virtual- (or average) crystal model of an alloy, where the height of the peak in the conduction-electron susceptibility, $\chi(\boldsymbol{q})$, is the weighted average of $\chi(\boldsymbol{q})$ for the constituents. For an alloy Ho:γ, this approach suggests that

$$T_N = x[xT_{Ho} + (1-x)T_\gamma] \quad , \tag{5}$$

where T_{Ho} is the transition temperature of pure Ho, and T_γ is the transition temperature of pure Ho assuming the conduction-electron susceptibility is that of pure γ. The solid lines in Fig. 8 are a fit of the data using Eq. (5) for γ= Y, Lu, and Sc. For Ho:Y and Ho:Lu, $T_{Ho} = 132 \pm 2$ K; with $T_\gamma = 144 \pm 2$ K, and 217 ± 3 K, respectively; while for Ho:Sc $T_{Ho} = 130 \pm 2$ K, and $T_\gamma = 53 \pm 2$ K. We conclude that the peak in $\chi(\boldsymbol{q})$ for Sc is smaller than that of Y or Lu. The transition temperature of Ho:Sc bulk alloys was also measured by Child and Koehler,[18] who in qualitative agreement with our own results found that T_N decreased with decreasing Ho concentration, and that for a given concentration, T_N was lower than that predicted by Eq. (4). However, Child and Koehler[18] also reported that T_N decreased rapidly for $x < 0.20$, and that for $x < 0.18$ there was no long-range magnetic order. Hence, in this low concentration region, there appears to be a difference between the behavior of the bulk alloys and our MBE-grown samples.

The temperature dependence of the wave vector for the $(002-q)$ peak for all samples is illustrated in Fig. 9. The wave vectors, $\boldsymbol{q} = \boldsymbol{q}_1$, at T_N are listed in Table III. $\boldsymbol{q}_1$ is of particular interest since in the limit of no magnetic ordering it gives the position of the peak in the conduction-electron

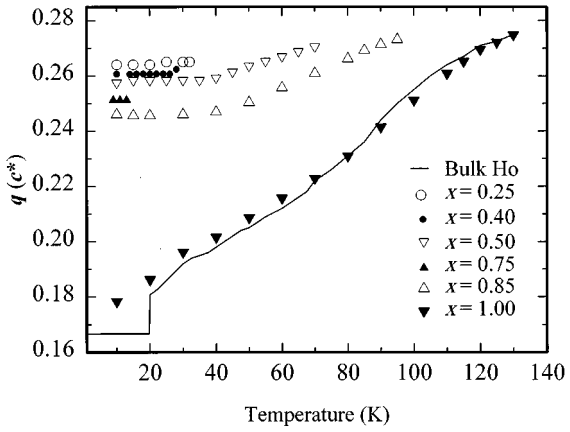

FIG. 9. The variation of ordering wave vector $\boldsymbol{q}$ with temperature for the alloy samples together, with that of bulk Ho.

susceptibility. Figure 10(a) shows the variation of $\boldsymbol{q}_1$ with x. A quadratic extrapolation to $x = 0.00$ gives the position of the peak in the Sc susceptibility as $\boldsymbol{q}_1 = 0.241 \pm 0.002\boldsymbol{c}^*$. This is comparable with results from other alloy systems containing Sc, for example Tb:Sc,[25] where it was found that $\boldsymbol{q}_1 \approx 0.23\boldsymbol{c}^*$. Child and Koehler[18] also studied the variation of $\boldsymbol{q}_1$ with concentration. Their results are less accurate than those we present, and there is agreement with our results within errors.

The wave vectors, $\boldsymbol{q} = \boldsymbol{q}_2$, measured at the lowest temperatures are listed in Table III and are commensurable with the crystal lattice. For most of the alloys, the wave vectors correspond to spin-slip structures based upon the commensurate $\boldsymbol{q} = (1/4)\boldsymbol{c}^*$ structure. These spin-slip structures are most easily described by giving the number of spin layers orientated along successive easy axes within the basal planes until the pattern repeats. In this notation, the $\boldsymbol{q} = (1/4)\boldsymbol{c}^*$ structure is denoted as (121), and the $\boldsymbol{q} = (1/6)\boldsymbol{c}^*$ structure is referred to as (2). For the alloys with $x = 0.4$, 0.5, and 0.75, the spin-slip

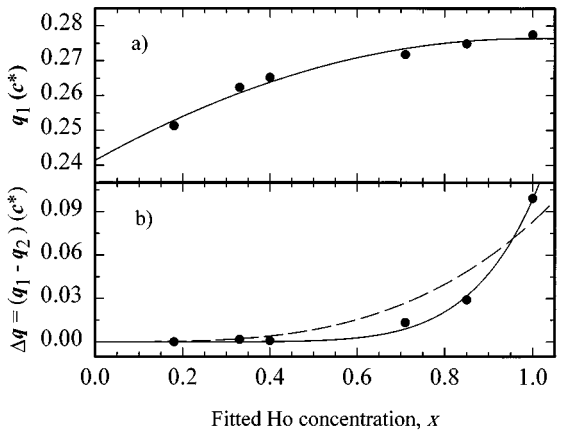

FIG. 10. (a) The dependence of the ordering wave vector $\boldsymbol{q}_1$ upon the fitted Ho concentration x. The quadratic fit to the data shown is extrapolated to the dilute limit of $x = 0.00$ to give $\boldsymbol{q}_1 = 0.241 \pm 0.002\boldsymbol{c}^*$. (b) The dependence of $\Delta\boldsymbol{q} = (\boldsymbol{q}_1 - \boldsymbol{q}_2)$ upon the fitted Ho concentration x. The solid line is a fit of the data to the power law $\Delta\boldsymbol{q} = Ax^n$, where $n = 7.0 \pm 0.5$. The dashed line is a fit with $n = 3.3$ found appropriate for Ho:Y and Ho:Lu alloys.

TABLE IV. The magnetic properties of Ho/Sc superlattices. The Néel temperatures T_N were calculated from the temperature dependence of the intensity of magnetic scattering measured at $(002-q)$. $\boldsymbol{q}_1$ and $\boldsymbol{q}_2$ (modulo 2π) are the wave vectors of the helical ordering at $T=T_N$ and $T=10$ K, respectively. The spin-slip structures formed at low temperatures are given in terms of the resulting fractional wave vector. The temperature-independent coherence lengths refer to magnetic ordering in the growth direction. The first length is for when the Ho moments are helically aligned within blocks, and the second for when they are ferromagnetically aligned. Finally, T_C is defined as the temperature at which additional magnetic scattering is first detectable in the region (002), upon cooling from $T>T_C$.

Nominal Ho/Sc	T_N K	$\boldsymbol{q}_{1(Ho)}$ $\pm 0.002\boldsymbol{c}^*$	$\boldsymbol{q}_{2(Ho)}$ $\boldsymbol{c}^*$	Spin-slip $\boldsymbol{c}^*$	$\boldsymbol{q}_{1(Sc)}$ $\pm 0.002\boldsymbol{c}^*$	$\boldsymbol{q}_{2(Sc)}$ $\boldsymbol{c}^*$	Coherence Å	length Å	T_C K
20/20	132 ± 5	0.258	0.170 ± 0.010	1/6	0.157	0.235 ± 0.010	135 ± 15,	250 ± 50	≈ 50
30/10	127 ± 2	0.261	0.174 ± 0.002	4/23	0.137	0.368 ± 0.002	150 ± 20,		
20/40	125 ± 3	0.267	0.181 ± 0.002	2/11			34 ± 15,		

structures have one (111) unit periodically replacing a (121) unit such that the structures formed are $((121)^5\ 111)$, $((121)^4\ 111)$, and $((121)^7\ 111)$, respectively. The spin-slip structure formed by the alloy with $x=0.85$ may also be based upon the $\boldsymbol{q}=(1/4)\boldsymbol{c}^*$ structure but with some of the (121) blocks replaced with a (212) block, resulting in the $((121)^{13}\ 212)$ spin-slip structure. Similar commensurate structures were also observed at low temperatures for Ho:Y (Ref. 22) and Ho:Lu (Ref. 5) alloys. For the alloys with $x=0.5$, 0.7, and 0.9, the spin-slip structures observed were $((121)^7\ 111)$, (121), (21); and $((121)^2\ 111)$, (121), (21) for Ho:Y and Ho:Lu, respectively.

The temperature dependence of the wave vector for the Ho film grown on a Sc-seed layer (i.e., the alloy sample with $x=1.0$) is similar to that of Ho films grown on Lu (Ref. 5) and Y.[22] For all of the Ho films, the wave vectors are larger or equal to those of bulk Ho. The magnetic structures formed by films with a thickness less than or equal to 5000 Å are basal-plane helices, except for the 5000 Å Ho film on a Lu-seed layer which showed evidence of a small ferromagnetic moment along the c axis below $T=20$ K. A 5000 Å Ho film grown on an Y-seed layer showed two commensurate structures at low temperatures corresponding to the $\boldsymbol{q}=(1/5)\boldsymbol{c}^*$ (21) and the $\boldsymbol{q}=(4/21)\boldsymbol{c}^*$ (2221) spin-slip structures. A Ho film of the same thickness but grown on a Lu-seed layer also showed two commensurate structures but these corresponded to the $\boldsymbol{q}=(1/6)\boldsymbol{c}^*$ (2), and the $\boldsymbol{q}=(7/39)\boldsymbol{c}^*$ (2222221) spin-slip structures. The thinner 2500 Å Ho film grown on a Sc-seed layer forms the $\boldsymbol{q}=(7/39)\boldsymbol{c}^*$ (2222221) structure at low temperatures. These results are consistent with the change in wave vector caused by the strain imposed on the Ho films by the different seed layers. For the Ho films on a Y-seed layer, the Ho a lattice parameters are larger than that of bulk Ho, while they are smaller for Ho films grown on Lu- and Sc-seed layers. Similarly, the c-axis parameters are smaller for Ho films with Y seed layers, and larger for the Lu- and Sc-seed layers. It is then initially surprising that for the films grown on Lu- and Sc-seed layers the wave vectors are larger than for bulk Ho. Presumably this arises because magnetoelastic effects in the basal plane increase the ordering wave vector and inhibit the development of the cone phase observed in bulk Ho.

Elliot and Wedgwood[26] suggested that $\Delta\boldsymbol{q}=(\boldsymbol{q}_1-\boldsymbol{q}_2)$ depends upon the band splitting produced by the ordered moments. Figure 10(b) illustrates the variation of $\Delta\boldsymbol{q}$ with fitted concentration, x. The solid line is a fit of the Ho:Sc data to the relation $\Delta\boldsymbol{q}=Ax^n$, where $n=7.0\pm0.5$. This is to be compared to the value of $n\approx3.3$, shown by the dashed line, found appropriate for Ho:Y and Ho:Lu alloys, as well as for bulk Ho.[5] The contrast in the exponents indicates that the changes in the band structure upon alloying Ho with Sc are different to the changes upon alloying with Y or Lu.

B. Ho/Sc superlattices

Neutron-diffraction techniques were used to investigate the magnetic structure of the superlattice samples. At $T=140$ K, when the wave-vector transfer is varied along $[00\ell]$ only the nuclear scattering is observed, as previously described in Sec. IV B. As the temperature is lowered, all the superlattices exhibit additional scattering at $(002\pm q)$, as illustrated in Fig. 6(a), indicating a basal-plane ordering of Ho moments. The temperature dependence of the intensity at $(002-q)$ was used to deduce values for T_N, which are listed in Table IV. The absence of any observable higher harmonics of the main magnetic scattering indicates that the helical structure is largely undistorted between $T=T_N$, and $T=4$ K. Scans with $\boldsymbol{Q}$ along $[10\ell]_{Ho}$ [with a typical example shown in Fig. 6(b)] establish that the moments are within error confined to the basal plane.

As for the nuclear scattering, it is interesting to compare the results of scanning $\boldsymbol{Q}$ along $[00\ell]$ and $[10\ell]_{Ho}$ as illustrated in Figs. 6(a) and 6(b), respectively. Along $[00\ell]$, the magnetic scattering at $(002-q)$ is structured, though the peaks are less well defined than those observed for Ho/Y (Ref. 20) or Ho/Lu (Ref. 5) superlattices. In contrast, along $[00\ell]_{Ho}$ the magnetic scattering at, say, $(101-q)$ has no structure and consists of a single peak that has a width corresponding approximately to one Ho block length.

While the samples Ho_{30}/Sc_{10} and Ho_{20}/Sc_{40} retain this type of helical order down to base temperature, the magnetic scattering observed from Ho_{20}/Sc_{20} changes considerably below $T\approx50$ K. Extra scattering is detected around the (002) structural peaks with an intensity that increases with decreasing temperature. Simultaneously, the intensity at the $(002-q)$ position reduces, falling to zero between $T=30$ and 20 K. A subtraction of data obtained from the same scan but with $T>T_N$ can be made for scans at temperatures below $T=50$ K. This subtraction yields a series of peaks around (002) separated by $2\pi/L$, but displaced by $2\pi/2L$ from the

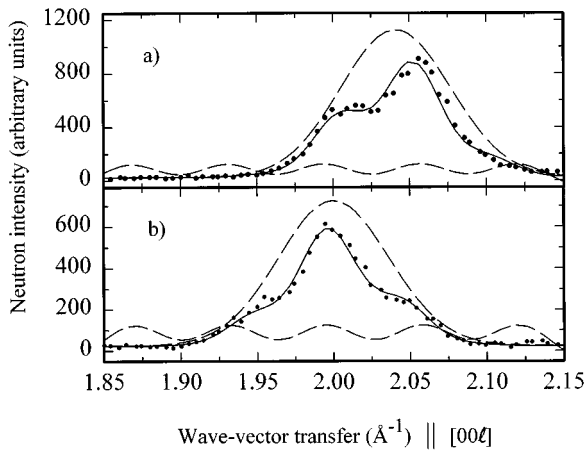

FIG. 11. Points show the neutron scattering observed at $T=4$ K from the superlattice Ho_{20}/Sc_{20} when $\boldsymbol{Q}$ is scanned along [00ℓ]. The solid line is the result of a subtraction of a similar scan for $T>T_N$, the latter scan having nuclear peaks at positions shown by the broken arrows. The remaining profile indicates a ferromagnetic arrangement of Ho moments within blocks, with an antiferromagnetic coupling between adjacent Ho blocks that is coherent over approximately 250 Å.

nuclear superlattice peak positions, as illustrated in Fig. 11. This profile corresponds to a ferromagnetic ordering of moments within the individual Ho blocks, but with adjacent Ho blocks antiferromagnetically coupled. This structure was also found in some Ho/Lu superlattices.[5] So while all three samples exhibit helical ordering at T_N, as the temperature is reduced Ho_{20}/Sc_{20} undergoes a transition beginning at $T\approx 50$ K to a mixed helical/ferromagnetic phase, with a pure ferromagnetic phase being established between $T=30$ and 20 K. The width of the peaks indicate that this antiferromagnetic coupling of ferromagnetically aligned Ho blocks is coherent over approximately 250 Å.

Although the moments in all the samples form a basal-plane spiral within *some* temperature region, the details of the helical ordering differ, and will now be considered more thoroughly. For a basal-plane helix, with the wave-vector transfer along [00ℓ], the intensity of the magnetic scattering from a superlattice structure, $I_{mag}(Q)$, is shown by Jehan *et al.*[20] to be given by

$$I_{mag}(Q)\propto|F(Q)|^2\left[\left(\sum_l J_l e^{i(QR_l-\beta_l)}\right)^2+\left(\sum_l J_l e^{i(QR_l+\beta_l)}\right)^2\right] , \quad (6)$$

where $F(Q)$ is the magnetic form factor, J_l is the basal-plane magnetic moment of the lth layer, R_l is the position of the lth atom along c, and β_l is the turn angle of the lth layer. l is summed over all planes in the superlattice. Factorizing the terms on the right-hand side of Eq. (6) gives

$$\sum_l J_l e^{i(QR_l\pm\beta_l)}=\sum_{m=1}^{N} e^{i(QLm\pm\Phi)}\times\sum_{l}^{\text{one bilayer}} J_l e^{i(QR_l\pm\beta_l)} , \quad (7)$$

where m is an integer, $\Phi=n_{Ho}\phi_{Ho}+n_{Sc}\phi_{Sc}$ is the total turn angle across one bilayer, and ϕ_{Ho} and ϕ_{Sc} are the turn angles per plane in Ho and Sc, respectively. For $N\rightarrow\infty$, the first term in Eq. (7) generates a series of δ functions at positions

$$Q_\pm=(2m\pi/L)\pm(\Phi/L) . \quad (8)$$

The amplitude of these δ functions is modulated by the second term, the one-bilayer structure factor, which for a model of only ordered Ho moments generates a profile centered at

$$Q_\pm=2m\pi/d_{Ho} . \quad (9)$$

The intensity of nuclear neutron scattering has the same functional form as Eq. (2), but with nuclear scattering lengths in place of x-ray form factors. Hence nuclear superlattice peaks occur at positions, Q_{Nuc}, given by Eq. (3). Combining Eqs. (3) and (8),

$$Q_{Nuc}-Q_-=\Phi/L . \quad (10)$$

Therefore the offset of the magnetic peaks from the position of the nuclear superlattice peaks gives Φ (modulo 2π).

A more detailed analysis of the magnetic scattering observed in the region $(002-q)$ can be made using Eq. (7) as a basis, which predicts magnetic peaks separated by $2\pi/L$. However, unlike previous superlattices such as Ho/Y (Ref. 20) and Ho/Lu,[5] the magnetic peaks for the Ho/Sc superlattices are less well defined and their separation is *not* equal to $2\pi/L$. For example, for Ho_{30}/Sc_{10}, the separation of the structural superlattice peaks is 0.063 ± 0.001 Å^{-1}, whereas the separation of the peaks magnetic peaks is 0.048 ± 0.002 Å^{-1}. We suggest that this difference arises because Eq. (7) has been derived assuming a magnetic structure with very long-range coherence. However, for a short-range coherence the series of δ functions generated by the first term in Eq. (7) are broadened, and there is a decrease in the separation of the resultant peaks observed in the magnetic-scattering profile. To account for such a short-range coherence, the series of peaks of separation $2\pi/L$ are modeled not as δ functions, but as equal amplitude Gaussians of *finite* width. The one bilayer structure factor is taken as a broad Gaussian peak to represent the scattering by the Ho moments. The width of this Gaussian corresponds to a single Ho block length, and hence can be obtained from the width of the scattering at the position of the $(101-q)_{Ho}$ peak (after correcting for the different resolution). The final profile around $(002-q)$ is then constructed from the product of a series of Gaussians of finite width, together with a single broad Gaussian. Figure 12 illustrates this approach for Ho_{30}/Sc_{10} at $T=10$ and 70 K.

Good fits to the data are obtained, with the total turn angle per bilayer, Φ, extracted from $Q_{Nuc}-Q_-$ using Eq. (10). ϕ_{Ho} can be deduced from the position of the broad Gaussian by applying Eq. (9), while the position of the $(101)_{Ho}$ peak provides an accurate value for d_{Ho}. Two unusual features are apparent. Firstly, although ϕ_{Ho} reduces on cooling (as in bulk Ho), Φ (modulo 2π) remains approximately constant. This is in contrast to Ho/Y (Ref. 20) and Ho/Lu (Ref. 13) superlattices, where both ϕ_{Ho} *and* Φ varied with temperature. Secondly, the series of Gaussians are positioned at approximately $2\pi/2L$ from the structural superlattice positions, so that $\Phi=(2m+1)\pi$. A quantitative example is provided

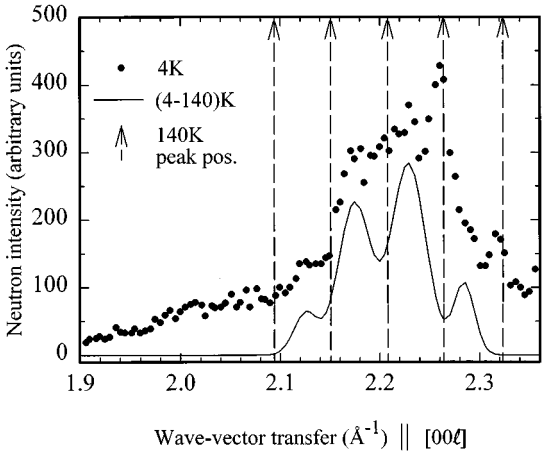

FIG. 12. Points illustrate the neutron scattering measured for $\boldsymbol{Q}$ scanned along [00ℓ] covering the region near $(002-q)$ for the superlattice sample Ho_{30}/Sc_{10} at (a) $T=10$ K, and (b) $T=70$ K. The dashed lines show a series of Gaussians separated by $2\pi/L$, together with a single broad Gaussian. The product of the series of Gaussians with the single broad Gaussian is used to construct the final profile shown by the solid line. The relative amplitude of the Gaussians is adjusted for clarity.

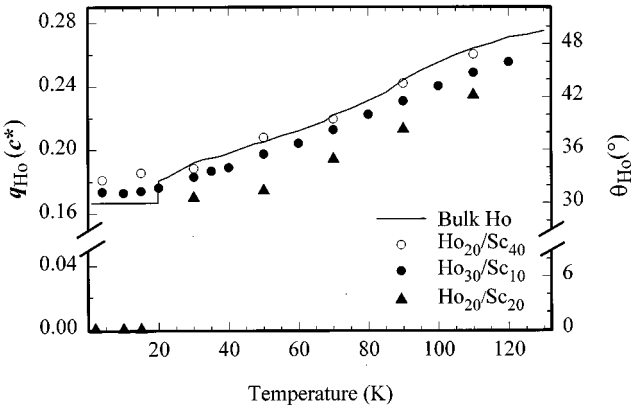

FIG. 13. The helical wave vector per plane in the Ho, $\boldsymbol{q}_{Ho}$ (ϕ_{Ho}), for the three superlattice samples, together with that of bulk Ho. $\boldsymbol{q}_{Ho}$ reduces to zero for sample Ho_{20}/Sc_{20} when the moments adopt a purely ferromagnetic arrangement.

by the results from Ho_{30}/Sc_{10}, for which the separation of the structural superlattice peaks is 0.063 ± 0.001 Å^{-1}. It is found that at *all* temperatures, $Q_{Nuc}-Q_{-}=0.343\pm0.005$ Å^{-1}, while the series of Gaussians are positioned at $2\pi/2L\pm0.005$ Å^{-1} from the structural superlattice positions. Final fits were obtained by constraining the position of the series of peaks to be at exactly $2\pi/2L$ from the structural superlattice peaks, with ϕ_{Ho} extracted as before. The values of ϕ_{Ho} at $T=T_N$ and $T=4$ K expressed as the wave vectors $\boldsymbol{q}_{1(Ho)}$, and $\boldsymbol{q}_{2(Ho)}$ are listed in Table IV. The width of the series of Gaussians can be used to deduce the coherence of the ordering, which is found to be temperature independent, and approximately equal to 1.4, and 1.3 bilayers for Ho_{30}/Sc_{10}, and Ho_{20}/Sc_{20}, respectively. For Ho_{20}/Sc_{40}, the width of the series of Gaussians indicates no coherence of the ordered Ho moments between adjacent Ho blocks. The data is therefore fitted to a broad Gaussian, the width of which is found to correspond approximately to one Ho block thickness. The lack of coherence of any type of magnetic ordering may be attributed to this sample possessing the largest number of Sc planes (nominally 40). Previous superlattice systems, such as Dy/Y,[27] have exhibited a reduction and final loss of coherent magnetic ordering with an increase in the nonmagnetic layer thickness, but the coherence persists for much greater distances than 40 planes. For Ho_{20}/Sc_{40}, ϕ_{Ho} can be obtained from an adaptation of Eq. (10) such that

$$Q_{(002)_{Ho}}-Q_{-}=\phi_{Ho}/d_{Ho}\ , \tag{11}$$

where the value for d_{Ho} obtained from the $(101)_{Ho}$ peak position can be used to calculate the position of $(002)_{Ho}$.

As seen from Fig. 13, above $T=20$ K the temperature dependence of ϕ_{Ho} for all samples resembles that of bulk Ho, with ϕ_{Ho} for a given temperature being slightly lower for the superlattices. This is in agreement with previous studies,[13] where it was found that coupling Ho together with an element of smaller a lattice parameter reduces the Ho turn angle. Below $T=20$ K, the moments in Ho_{20}/Sc_{20} are aligned ferromagnetically, with $\phi_{Ho}=0$. The minimum wave vector that can be extracted from the mixed helical/ferromagnetic phase is, within error, the commensurate value $\boldsymbol{q}=(1/6)\boldsymbol{c}^*$. For Ho_{30}/Sc_{10}, and Ho_{20}/Sc_{40}, ϕ_{Ho} locks in to values commensurable with the crystal lattice, with the formation of the $\boldsymbol{q}=(4/23)\boldsymbol{c}^*$ (22222221), and the $\boldsymbol{q}=(2/11)\boldsymbol{c}^*$ (222221) spin-slip structures, respectively.

As a cross reference, ϕ_{Ho} for all samples can be extracted from the measurements obtained by scanning $\boldsymbol{Q}$ along $[10\ell]_{Ho}$ at different temperatures. Again adapting Eq. (10), it follows that

$$Q_{(101)_{Ho}}-Q_{(101-q)_{Ho}}=\phi_{Ho}/d_{Ho}\ . \tag{12}$$

Within errors, the same results are obtained as from the [00ℓ] data.

Since $\Phi=n_{Ho}\phi_{Ho}+n_{Sc}\phi_{Sc}$, it is possible to obtain a value for ϕ_{Sc}, the effective turn angle per plane in the Sc blocks. Given the variation of ϕ_{Ho} illustrated in Fig. 13, and the constancy of Φ, it is clear that ϕ_{Sc} falls with increasing temperature, and with a different temperature dependence for each superlattice. Furthermore, the wave vectors upon ordering, $\boldsymbol{q}_{1(Sc)}$, tabulated in Table IV, do not agree with the value of $\boldsymbol{q}_{1(Sc)}=0.241\pm0.002\boldsymbol{c}^*$ obtained from an extrapolation to $x=0.00$ of measurements from the Ho:Sc alloys. These results emphasize that the magnetic properties of Ho/Sc differ from superlattices with Y or Lu interlayers; such as Ho/Y (Ref. 20) and Ho/Lu;[5] or Dy/Y (Ref. 11) and Dy/Lu.[28]

VI. DISCUSSION

The structural investigations of the Ho-Sc alloys and superlattices reveal, in both cases, that the samples did not grow pseudomorphically and that in particular there exist different a lattice parameters for the superlattice constituents. While studies of the relationship between rare-earth epitaxial growth and lattice mismatch are not numerous, there have been many reports detailing the epilayer growth of semiconductors upon substrates. In one such report by Jain *et al.*,[29] it is shown how the elastic energy stored in an epilayer due to

homogeneous strain is proportional to the thickness of the epilayer t. As t increases and exceeds a critical thickness, t_c, misfit dislocations set in, with a concomitant departure from pseudomorphic growth. Theories have been developed, most notably those by Franck and van der Merwe,[30] and Matthews,[31] to calculate t_c. It is found that t_c is proportional to the size of the lattice mismatch between the two layers. Although details are based upon specific semiconductor systems, general conclusions can still be drawn for Ho-Sc. Clearly the observed difference in a lattice parameters indicates that $t > t_c$ for all the samples studied. Also, it should be noted that while the large lattice mismatch for Ho-Sc might at first suggest a highly strained system, the separation of in-plane parameters means the lattice has relaxed, most probably with the introduction of misfit dislocations, and a concomitant reduction in overall strain. For the Ho/Sc superlattices, it is the presence of such dislocations at the many interfaces that may account for the unusually large mosaic spread values. A comparison of the fitted Ho lattice parameters for Ho/Sc with those of Ho/Lu,[13] shows the difference from bulk values for both systems are of a similar magnitude, despite the mismatch in Ho/Sc being many times greater than that of Ho/Lu (Sec. I). The structural properties are therefore important when qualitatively assessing the magnitude of strain in a system, which in turn can affect the magnetic properties.[32]

The $4f$ moments in the alloy samples order in a helix, with the moments confined to the basal plane. This is consistent with $\chi(\boldsymbol{q})$ having a peak at a wave vector along the c axis, with the moments confined to the basal plane by the crystal field.[33] The form of the dependence of T_N upon concentration cannot be accounted for by a model in which $\chi(\boldsymbol{q})$ is independent of the rare-earth ion.[4] As for Ho:Y and Ho:Lu,[5] a good description is given by an average crystal model in which $\chi(\boldsymbol{q})$ is considered to vary linearly between the two alloy constituents. For the virtual-crystal model outlined in Sec. V A, T_{Sc} is found to be less than T_{Ho}, T_Y, or T_{Lu}. This result is in accord with calculations,[10,33] that suggest the peak in $\chi(\boldsymbol{q})$ for Sc is smaller than that of Ho, Y, or Lu.

Broad trends in the ordering wave vector $\boldsymbol{q}$ are also in agreement with results from Ho:Y and Ho:Lu alloys,[5] with the dependence of $\boldsymbol{q}$ upon temperature being enhanced as the Ho concentration increases. The occurrence of spin-slip structures, as in bulk Ho,[15] reflects a compromise between ordering with a wave vector favored by the exchange energy, while still aligning moments close to easy axes produced by the crystal field. The increase in width of the $(002-q)$ peak at $T=10$ K indicates the competition between the exchange and crystal-field energies. Whilst there may be on average 13 planes between spin slips, the structure is not perfectly regular. It is interesting to note that for a given x, similar spin-slip structures are formed in Ho:Sc as were detected in Ho:Y and Ho:Lu,[5] suggesting that at very low temperatures, the ordering wave vector is not qualitatively affected by the differences between the nonmagnetic components. However, in more detail, if it is assumed that the change in the wave vector, $\Delta\boldsymbol{q}=(\boldsymbol{q}_1-\boldsymbol{q}_2)$, with temperature depends on the ordered moment at low temperature, which is proportional to x, then for Ho:Sc alloys $\Delta\boldsymbol{q}$ is proportional to the moment to the power of 7.0 ± 0.5, compared to the power of approximately 3.3 found for Ho:Y and Ho:Lu,[5] and also bulk Ho. Although no quantitative explanation has yet been given for the latter exponents, it is clear that if the temperature dependence of the ordering wave vector arises from the effect of magnetic order on the band structure,[26] then the changes in the Ho band structure on introducing Sc are different to those arising from the introduction of either Y or Lu.

The moments in all three superlattice samples also form basal-plane helices at T_N. However, unlike any of the alloy samples, for the Ho_{20}/Sc_{20} superlattice there is a transition at $T\approx50$ K to a mixed helical/ferromagnetic phase, followed by the establishment of a pure ferromagnetic phase between $T=30$ and 20 K. The minimum wave vector, $\boldsymbol{q}=\boldsymbol{q}_{2(Ho)}$, obtained from the mixed helical/ferromagnetic phase is $\boldsymbol{q}=0.170\pm0.010\boldsymbol{c}^*$, which is consistent with the commensurate value of $\boldsymbol{q}=(1/6)\boldsymbol{c}^*$. This is in agreement with the results from Ho/Lu (Ref. 5) superlattices, and also the theoretical work of Seno *et al.*[34] who suggest that $\boldsymbol{q}=(1/6)\boldsymbol{c}^*$ is the lowest value possible for the helical wave vector, with the only stable state at low temperatures for $\boldsymbol{q}<(1/6)\boldsymbol{c}^*$ being a ferromagnet. A study by Andrianov[35] suggests the period of helical magnetic structures in heavy rare earths depends upon the ratio of the lattice parameters c/a, with a transition to a ferromagnetic structure expected when the ratio exceeds 1.582. To an accuracy of ±0.005, the values of c/a at $T=4$ and 140 K are 1.580 and 1.574; 1.614 and 1.585; and 1.569 and 1.562 for the samples Ho_{30}/Sc_{10}, Ho_{20}/Sc_{20}, and Ho_{20}/Sc_{40}, respectively. Hence, within errors, the results of our measurements of c/a are in agreement with Andrianov's predictions. The fitted structural parameters further suggest that Ho_{20}/Sc_{20} is the most strained of the three superlattices. Not only does this sample have the greatest difference between the fitted d spacings for Ho and Sc (Table II), but it is also the only sample to have a value for d_{Ho} that corresponds to a value for the c lattice parameter that is greater than that of bulk Ho.[12]

The details of the helical ordering of the Ho/Sc superlattices differ considerably from superlattices such as Ho/Y (Ref. 20) and Ho/Lu.[13] Firstly, for the Ho/Sc superlattices the coherence length associated with the helical ordering is at most 1.5 bilayers, compared with coherence lengths over many bilayers observed for Ho/Y and Ho/Lu. Secondly, $\Phi=(2m+1)\pi$ at all temperatures. Since ϕ_{Ho} changes with temperature as shown in Fig. 13, this implies that ϕ_{Sc} must have an equal and opposite temperature dependence. Furthermore, ϕ_{Sc} is very different from that deduced from the peak in the electronic susceptibility as determined by either the Ho:Sc alloy measurements (Sec. III A), or by theoretical calculations.[36,37]

These results also differ from those obtained for Ho/Pr (Ref. 8) superlattices, which showed no coherence of helically ordered Ho moment over Pr blocks, even for Pr blocks only six layers thick. It is also of interest to compare our results with those obtained from Dy/Sc (Ref. 9) superlattices. It was reported that there was no coherent ordering of Dy moments over Sc interlayers, although the data may allow for the possibility of a short-range coherent ordering similar to that observed for the Ho/Sc superlattices.

The magnetic interactions in many previous rare-earth superlattice systems[6,11,20] were described as being mediated by conduction electrons. In terms of such interactions, two ob-

servations might explain the short-range coherence lengths observed for the Ho/Sc superlattices. Firstly, the large number of structural defects associated with the existence of different a lattice parameters might reduce the conduction-electron mean free path. Secondly, calculations[36,37] suggest that although qualitatively similar, the peak in $\chi(\boldsymbol{q})$ for Sc is in detail smaller and probably broader than those of, say, Ho or Y, leading to shorter-range coherence lengths for Ho/Sc.

This second observation is also important when considering the temperature dependence of ϕ_{Sc}, in addition to the fact that qualitatively ϕ_{Sc} differs from both the values expected from the Ho:Sc alloy studies, and from theoretical calculations. A small and probably broad peak in $\chi(\boldsymbol{q})$ might suggest that ϕ_{Sc} will be dependent on the detailed environment of the Sc, and be particularly influenced by strain. These characteristics of $\chi(\boldsymbol{q})$ allow the possibility of the temperature variation observed for ϕ_{Sc}, and also for the fact that the magnetic interactions through the Sc layers in the superlattice system cannot be predicted from the corresponding alloy study, or from calculations based upon bulk Sc.

The observation that Φ is not only constant at all temperatures, but specifically that $\Phi=(2m+1)\pi$, indicates that there is an overall antiferromagnetic coupling between adjacent Ho blocks. We suggest an explanation for this, yet to be fully developed, based on the possible influence of dipolar interactions. If each Ho block has a net ferromagnetic moment, magnetic dipolar forces would align these net moments antiferromagnetically between adjacent Ho blocks, accounting for the observed values of Φ. We have estimated the net field in the center of a Ho block arising from two nearest-neighbor antiferromagnetically aligned planes. The magnetic domains were taken to be circular with a radius of 90 Å obtained from the width of the magnetic scattering in the basal plane. The net moment of a Ho block depends on its width and ϕ_{Ho}, but typically the field is found at low temperatures to be a maximum of the order 0.03 T. Since this field is much smaller at T_{N}, it seems unlikely that it is sufficiently strong to cause the observed ordering at high temperatures. Furthermore, it is difficult to understand why the dipolar forces have more of an effect in Ho/Sc superlattices than in Ho/Pr (Ref. 8) superlattices. If the samples were to be placed in an applied field sufficiently strong to overcome the dipolar forces, it should be found that $\Phi=2m\pi$. We plan measurements to test this prediction in the near future.

To summarize, we have studied the structural and magnetic properties of Ho-Sc alloys and superlattices grown by MBE. Structural investigations reveal the existence of different a lattice parameters that has not been reported, to our knowledge, for previous rare-earth MBE grown systems. When considering the magnetic properties there is not only a contrast between the Ho-Sc alloys and superlattices themselves, but they compare in differing ways to previously studied systems. For the alloys, it is found that there is long-range coherence of the magnetic structures formed. ϕ_{Ho} is greater than in bulk Ho, and no ferromagnetic structures are observed. The spin-slip structures identified are similar to those found in Ho:Y and Ho:Lu alloys. Also in accord with Ho:Y and Ho:Lu, a good qualitative description of the overall magnetic properties is given by a virtual-crystal model. For the superlattices, only magnetic structures with a relatively short-range coherence are formed. ϕ_{Ho} is in general less than in bulk Ho, and a basal plane ferromagnetic structure is observed for the most strained sample. The spin-slip structures identified differ from those found in Ho/Y or Ho/Lu superlattices. Also in contrast to superlattices with Y or Lu interlayers, there is no long-range coherence of helically ordered Ho moments over the nonmagnetic interlayers. Some of the unusual characteristics of the helical ordering might be accounted for by a consideration of the structural properties, band-structure calculations, and the possible influence of dipolar forces.

ACKNOWLEDGMENTS

We would particularly like to acknowledge many useful discussions with the late A.R. Mackintosh and advice from J.A. Simpson. The work in Oxford was funded by the EPSRC, and the experiments at Risø by the EU through the Large Installation Programme. C.B.-J. is grateful for the financial support of the EPSRC.

[1] C.F. Majkrzak, J. Kwo, M. Hong, Y. Yafet, D. Gibbs, C.L. Chien, and J. Bohr, Adv. Phys. **40**, 99 (1991).
[2] J.J. Rhyne, M.B. Salamon, C.P. Flynn, R.W. Erwin, and J.A. Borches, J. Magn. Magn. Mater. **129**, 39 (1994).
[3] R.A. Cowley, D.F. McMorrow, P.P. Swaddling, R.C.C. Ward, and M.R. Wells, Ind. J. Pure Appl. Phys. **33**, 509 (1995).
[4] H.R. Child, W.C. Koehler, E.O. Wollan, and J.W. Cable, Phys. Rev. **138**, A1655 (1965).
[5] P.P. Swaddling, R.A. Cowley, R.C.C. Ward, M.R. Wells, and D.F. McMorrow, Phys. Rev. B **53**, 6488 (1996).
[6] Y. Yafet, J. Appl. Phys. **61**, 4058 (1987).
[7] J.A. Simpson, D.F. McMorrow, D.A. Jehan, R.A. Cowley, M.R. Wells, R.C.C. Ward, and K.N. Clausen, Phys. Rev. Lett. **73**, 1162 (1994).
[8] J.A. Simpson, D.F. McMorrow, R.A. Cowley, M.R. Wells, and R.C.C. Ward, J. Phys. Condens. Matter **7**, L417 (1995).
[9] F. Tsui, C.P. Flynn, R.S. Beach, J.A. Borches, R.W. Erwin, and J.J. Rhyne, J. Appl. Phys. **73**, 6904 (1993).
[10] S.H. Lui, R.P. Gupta, and S.K. Sinha, Phys. Rev. B **4**, 1100 (1971).
[11] M.B. Salamon, J. Borches, S. Sinha, R. Du, J.E. Cunningham, and C.P. Flynn, Phys. Rev. B **35**, 6808 (1987).
[12] R.W.G. Wyckoff, *Crystal Structures* (Interscience, New York, 1965), Vol. 1.
[13] D.F. McMorrow, D.A. Jehan, P.P. Swaddling, R.A. Cowley, R.C.C. Ward, M.R. Wells, and K.N. Clausen, Physica B **192**, 150 (1993).
[14] W.C. Koehler, J.W. Cable, M.K. Wilkinson, and F.O. Wollan, Phys. Rev. **151**, 414 (1966).
[15] D. Gibbs, D.E. Moncton, K.L. D'Amico, J. Bohr, and B.H. Grier, Phys. Rev. Lett. **55**, 234 (1985).
[16] R.A. Cowley and S. Bates, J. Phys. C **21**, 4113 (1988).
[17] J.A. Simpson, D.F. McMorrow, R.A. Cowley, and J.A. Jehan, Phys. Rev. B **51**, 16 073 (1995).

[18] H.R. Child and W.C. Koehler, Phys. Rev. **174**, 562 (1968).
[19] J. Kwo, E.M. Gyorgy, D.B. McWhan, F.J. DiSalvo, C. Vettier, and J.E. Bower, Phys. Rev. Lett. **55**, 1402 (1985).
[20] D.A. Jehan, D.F. McMorrow, R.A. Cowley, M.R. Wells, R.C.C. Ward, N. Hagman, and K.N. Clausen, Phys. Rev. B **48**, 5594 (1993).
[21] P.P. Swaddling, D.F. McMorrow, R.A. Cowley, R.C.C. Ward, and M.R. Wells, Phys. Rev. Lett. **73**, 2232 (1994).
[22] R.A. Cowley, R.C.C. Ward, M.R. Wells, M. Matsuda, and B. Sternlieb, J. Phys. Condens. Matter **6**, 2985 (1994).
[23] J.P. Goff, C. Bryn-Jacobsen, D.F. McMorrow, R.A. Cowley, R.C.C. Ward, and M.R. Wells (unpublished).
[24] G.P. Flecher, G.H. Lander, T. Ari, S.K. Sinha, and F.H. Spedding, Phys. Rev. B **13**, 3034 (1976).
[25] H.R. Child and W.C. Koehler, J. Phys. **37**, 1353 (1966).
[26] R.J. Elliott and F.A. Wedgwood, Proc. Phys. Soc. London **84**, 63 (1964).
[27] J.J. Rhyne, R.W. Erwin, J.A. Borches, S. Sinha, M.B. Salamon, R. Du, and C.P. Flynn, J. Appl. Phys. **61**, 4043 (1987).
[28] R.S. Beach, J.A. Borches, R.W. Erwin, C.P. Flynn, A. Mathney, J.J. Rhyne, and M.B. Salamon, J. Magn. Magn. Mater. **104-107**, 1915 (1992).
[29] S.C. Jain, A.H. Harker, and R.A. Cowley (unpublished).
[30] F.C. Franck and J. van der Merwe, Proc. R. Soc. London Ser. A **198**, 216 (1949).
[31] J.W. Matthews, in *Epitaxial Growth B*, edited by J.W. Matthews (Academic, New York, 1975).
[32] J.A. Borchers, M.B. Salamon, R.W. Erwin, J.J. Rhyne, R. Du, and C.P. Flynn, Phys. Rev. B **43**, 3123 (1991).
[33] J. Jensen and A.R. Mackintosh, *Rare Earth Magnetism - Structures and Excitations* (Oxford Science, New York, 1991).
[34] F. Seno, J.M. Yeomans, R. Harbord, and D.Y.K. Ko, Phys. Rev. B **49**, 6412 (1994).
[35] A.V. Andianov, JETP Lett. **55**, 667 (1992).
[36] J. Rath and J.A. Freeman, Phys. Rev. B **11**, 2109 (1975).
[37] R.P. Gupta and A.J. Freeman, Phys. Rev. B **13**, 4376 (1976).